

RESEARCH ARTICLE

Synthesization and characterization of SnCaAl₂O₃ nanocomposite and using as a superior adsorbent for Pb, Zn, and Cd ions in polluted water

Ali Sayqal¹, Moustafa Gamal Snousy², Mahmoud F. Mubarak³, Ahmed H. Ragab⁴, Atef Mohamed Gad Mohamed^{5*}, Abeer El Shahawy^{6*}

1 Department of Chemistry, Faculty of Applied Science, Umm-Al-Qura University, Makkah, Saudi- Arabia, **2** Egyptian Petroleum Sector, Petrotrade Co., Cairo, Egypt, **3** Petroleum Applications Department, Egyptian Petroleum Research Institute (EPRI), Cairo, Egypt, **4** Department of Chemistry, Faculty of Science, King Khalid University, Abha, Saudi Arabia, **5** Assiut & New Valley Company for Water and Wastewater, Assiut, Egypt, **6** Department of Civil Engineering, Faculty of Engineering, Suez Canal University, Ismailia, Egypt

* abeer_shahawi@eng.suez.edu.eg (AES); atefgad98@yahoo.com (AMGM)



OPEN ACCESS

Citation: Sayqal A, Snousy MG, Mubarak MF, Ragab AH, Mohamed AMG, El Shahawy A (2022) Synthesization and characterization of SnCaAl₂O₃ nanocomposite and using as a superior adsorbent for Pb, Zn, and Cd ions in polluted water. PLoS ONE 17(11): e0276888. <https://doi.org/10.1371/journal.pone.0276888>

Editor: Moonis Ali Khan, King Saud University, SAUDI ARABIA

Received: September 6, 2022

Accepted: October 16, 2022

Published: November 3, 2022

Peer Review History: PLOS recognizes the benefits of transparency in the peer review process; therefore, we enable the publication of all of the content of peer review and author responses alongside final, published articles. The editorial history of this article is available here: <https://doi.org/10.1371/journal.pone.0276888>

Copyright: © 2022 Sayqal et al. This is an open access article distributed under the terms of the [Creative Commons Attribution License](https://creativecommons.org/licenses/by/4.0/), which permits unrestricted use, distribution, and reproduction in any medium, provided the original author and source are credited.

Data Availability Statement: All relevant data are within the paper and its [Supporting information](#) files.

Abstract

The presence of heavy metals in drinking water or wastewater poses a serious threat to the ecosystem. Hence, the present study focused on synthesizing SnCaAl₂O₃ core-shell nanoparticles (C.N.P.s) in the α-Alumina phase by thermal annealing a stacked structure sandwiched between two Al₂O₃ layers at low temperatures. The obtained structure showed Sn N.P. floating gate with an Al₂O₃ dielectric stacked tunneling barrier to remove the excess of these heavy metals from polluted water. To characterize the prepared composites, X-ray diffraction (XRD), field emission scanning electron microscope (FE-SEM), and high-resolution transmission electron microscopy (HR-TEM) were used. The synthesized SnCaAl₂O₃ C.N.P.s composite was examined to utilize it as an adsorbent for removing Zn, Cd, and Pb divalent cations. The removal efficiency was studied by various parameters such as adsorbent dose, pH, contact time, metal concentrations, temperature, and coexisting ions. The experimental results were tested via Langmuir and Freundlich isotherm models. The obtained results were convenient to the Freundlich isotherm model. Moreover, the adsorption thermodynamic behavior of Zn⁺², Cd⁺², and Pb⁺² on the synthesized composite was examined, and the process is endothermic and spontaneous under experimental conditions. The results illustrated that the adsorption efficiency of the SnCaAl₂O₃ core-shell nanoparticles (C.N.P.s) ranged from 88% to about 100% for all cations.

1. Introduction

Water pollution by toxic heavy metal ions is a critical environmental problem that may pose serious health effects. The dissolved metal ions do not undergo decomposition in nature, resulting in significant health hazards to humans and the ecosystem [1–4]. Mining and

Funding: The authors would like to thank the Dean of Science and Research at King Khalid University for giving financial support via the General Research Project: grant no. (R.G.P.1/28/43), Saudi Arabia. And The authors would like to thank the Deanship of Scientific Research at Umm Al-Qura University for supporting this work by Grant Code: (22UQU4280446DSR02).

Competing interests: The authors have declared that no competing interests exist.

smelting operations, industrial production/usage, residential wastes, sewage discharge, and agriculture are the primary sources of heavy metals in the environment [5–8].

Among heavy metals, Zn⁺², Cd⁺², and Pb⁺² ions are commonly available in industrial wastewater [9]. Biogeochemical cycles introduce these elements into the food chain as toxins. Causes highly poisonous and tends to concentrate in muscle and fatty tissues. Heavy metals can pass through the water stream, air, and soil for long distances, so it is too difficult to assess their impact on the environment [10]. Heavy metals can stand stable for many years without decomposition resulting in various risks [11–13]. Heavy metals removal from wastewater can be applied using different techniques such as ion exchange, reverse osmosis, separation with flotation, adsorption, and absorption.

The common removal system is the adsorption of ions on the surface of many solid materials such as clay, zeolites, activated charcoal, or silica gel. These solid materials have suitable properties, such as large pore volumes, large surface area, high porosity, and high exchange capacity for cations [14, 15]. Supercapacitor electrode materials that include transition metal oxides, phosphides, hydroxides, conductive polymers, and layers of hydroxides and selenides are commonly employed [16–18]. But these different adsorbent materials cannot produce large amounts of treated water. They must be used in huge quantities of these materials to obtain the required quantities of treated water [19–22]. It is known that nanoparticles of calcium oxide (CaO) and (CaAl₂O₃) appear to have unique properties due to their high adsorption capacity and their high catalytic activity [23]. On another side, the nanocomposites of SnAl₂O₃ are characterized by a large surface area due to the encasement of Al in the SnO₂ lattice, which would generate an interstitially solid solution, causing composite surface area to increase [24].

This work aims to manufacture SnCaAl₂O₃ core-shell nanoparticles, and this material is SnAl₂O₃ as a strong adsorbent and (CaAl₂O₃) as a potent catalyst. So, SnCaAl₂O₃ composite has superior efficiency and can adsorb heavy metal cations. Furthermore, the absorption properties and absorption mechanisms of the prepared composite SnCaAl₂O₃ were studied to remove Zn⁺², Cd⁺², and Pb⁺², as well as mixtures of solutions.

2. Materials and method

2.1. Materials

Zinc chloride heptahydrate (ZnCl₂·7H₂O), lead sulfate pentahydrate (PbSO₄·5H₂O), cadmium sulfate heptahydrate (CdSO₄·7H₂O), and calcium chloride hexahydrate (CaCl₂·6H₂O) all are analytically pure, (Federal Standard 4528–78), and aluminum nitrate (Al(NO₃)₃), chemically pure, Sigma Aldrich, were used to prepare the starting aqueous solutions of CTAB (98% purity, Sigma Aldrich, St. Louis, MO, U.S.A.), CaCl₂, SnCl₂ (98% purity, Alfa Aesar, Haverhill, MA, U.S.A.), and NH₄OH (25% purity, Union Chemical Works Ltd., Kaohsiung, Taiwan).

2.2. Preparation of Al₂O₃ nanoparticles

Al₂O₃ within the SnCaAl₂O₃ core-shell nanoparticles (C.N.P.s) was prepared using the sol-gel technique [25]. Al(NO₃)₃ was dissolved in a proper volume of glacial acetic acid with continuous stirring while heating on a hot plate for 3 h at 80°C. After that, a small volume of polyvinyl alcohol was poured into this solution. The resulting solution was left for another 6 h with the same conditions of stirring and heating [26]. After elapsing this time, the mixture was centrifuged at 3000 rpm for 10 min, washed for many periods with deionized water and ethanol, and dried using an oven dryer at 80°C for 12 h. Furthermore, the dried powder grounded well and hardened at 700°C for 3 h in the air using a muffle furnace to produce pure nano Al₂O₃ layers [27].

2.3. Preparation of SnCaAl₂O₃ Core-Shell Nanoparticles

A known amount of the as-prepared nano Al₂O₃ shells was first dispersed in 20 mL of deionized water, followed by a pre-determined amount of CTAB, CaCl₂, and SnCl₂ with stirring and heating at 300 rpm at 40°C for 2 h, respectively. After mixing well, NH₄OH solution was slowly added for pH adjustment of the mixture to reach 10 and left for 12 h [28], then centrifuged at 2000 rpm [29, 30]. The produced solid particles were dried for 24 h at 110°C and calcined in atmospheric air at a specific temperature for 3 h [31].

2.4. SnCaAl₂O₃ characterization

X-ray diffraction (XRD) spectra for SnCaAl₂O₃ sample captured via a powder diffractometer (Ultima IV, Rigaku Corp., Tokyo, Japan) and Cu-K radiation. Emission scanning electron microscopy (FE-SEM) with a speeding voltage of 5 kV and a current of 10 A (S-4500, Hitachi Ltd., Tokyo, Japan) and high-resolution transmission electron microscopy (HR-TEM) were used to recognize the morphological structure of the samples. HR-TEM pictures were acquired by dispersing the sample powder in ethanol and depositing it on a copper grid. The FT/IR-4100 spectrometer (Jasco Corp., Hachioji, Japan) was used to generate FT-IR spectra with a resolution of 2.0 cm⁻¹ in the wavelength range of 4000–400 cm⁻¹.

2.5. Heavy metals adsorption by SnCaAl₂O₃ core-shell nanoparticles

The sorption characteristics of the as-synthesized SnCaAl₂O₃ C.N.P.s were determined using the technique of limited volume at room temperature (20 ± 2°). In comparison, samples of SnCaAl₂O₃ C.N.P.s (S) were stirred in Erlenmeyer flasks with different concentrations of heavy metals (L) ranging from 50 up to 500 mg/L, with the ratio of S:L = 1:5 for 4 h using a lab shaker [32]. The solid adsorbent was then removed from the liquid by centrifugation and filtration. To estimate the Zn⁺², Cd⁺², and Pb⁺² cations contents, analytical atomic absorption spectroscopy (AA-6300, Shimadzu, Kyoto, Japan) was used. The gotten data are the average of three independent experiments. The sorption properties of the used material can be explained using Eq 1, where Q_{eq} (mg_{eq}/g) is the static exchange capacity, C_0 is the initial concentration, and C_t is the steady-state concentration (mg/L). V is the metal ions volume in solution (L), and m is the sorbent weight (g) [33].

$$Q_{eq} = (C_0 - C_t) \times \frac{V}{m} \quad (1)$$

In this study, several influences have been examined, such as contact time (10–80 min), pH (2–9), the dosage of adsorbent (0.02 g up to 1 g), metal ions concentration (50–500 mg/L), the effect of temperature (25–66°C), and effect of coexisting ions Na⁺ and Ca²⁺.

3. Results and discussions

Due to the dangers of heavy metals to the ecosystem, many scientists and researchers have worked hard to find effective and quick solutions to confront these pollutants; [34] examined the use of multiwalled carbon nanotubes (MCNTs) to remove fenuron pesticide from wastewater, [35] used a new method and technique in treating sludge by removing water from sludge using Extracellular polymeric substances (EPS) [36–41].

The present study discussed the novel preparation and characterization of SnCaAl₂O₃ Nanocomposite material via different characterization techniques. On another side, it examined this new synthetic material as a superior adsorbent to remove heavy metals (Zn⁺², Cd⁺², and Pb⁺²) in the wastewater as a new application.

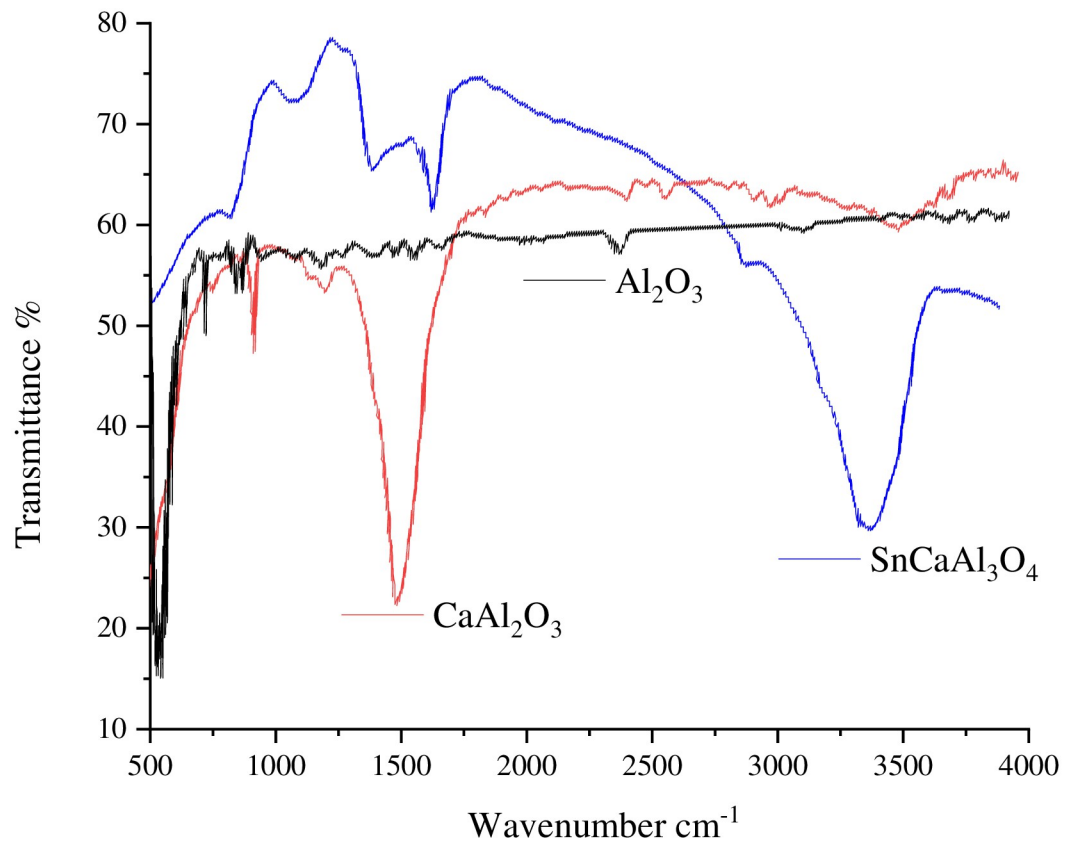


Fig 1. FTIR of Al₂O₃, CaAl₂O₃, and SnCaAl₂O₃ nanoparticles.

<https://doi.org/10.1371/journal.pone.0276888.g001>

3.1. Alumina nanoparticles characterization

3.1.1. FTIR spectroscopy. FTIR spectrum examination was applied to identify the surface functional groups of the prepared nanoparticles (Fig 1). Fig 1 illustrates that the 3457 cm⁻¹ peak is related to the O–H group expansion vibration related to the Al–O–H framework. The 1629 cm⁻¹ peak is related to the water molecules which are adsorbed physically at the adsorbent surface [42]. In contrast, the wavelength-wide pattern range of 400–1000 cm⁻¹ distinguishes and indicates the creation of the γ -phase alumina [43].

Moreover, the sorption bands of the Al–O–Al bond at 911, 804, and 637 cm⁻¹ are indexed to asymmetric/symmetric stretching and bending vibration [24, 44, 45]. The peak below 700 cm⁻¹ corresponds to Al⁺³ octahedral arrangement in the SnCa-oxide hcp lattice. At the same time, the peaks between 700 and 950 cm⁻¹ represent the C.C.P. lattice tetrahedral sites of the oxide ions occupied with Al⁺³ ions [42]. So, the produced γ -alumina phase coordinates octahedral and tetrahedral units [46].

3.1.2. Thermal analysis. TG-DTA analysis investigated the sample's thermal behavior (Fig 2). The sample's T.G. curve showed three weight decreases. Firstly, at 148°C, the initial sample weight loss was nearly 11%. This weight loss correlates with the D.T.A. profile exothermic peak, representing the desorption of physically adsorbed water. Between 150 and 300°C, a second large weight loss of nearly 34% is attributable to removing ethanol and other impurities [47]. The last notable weight loss is the third, representing 65% of the total weight loss and occurs at 375°C, accompanying a strong D.T.A. exothermic peak and is attributed to

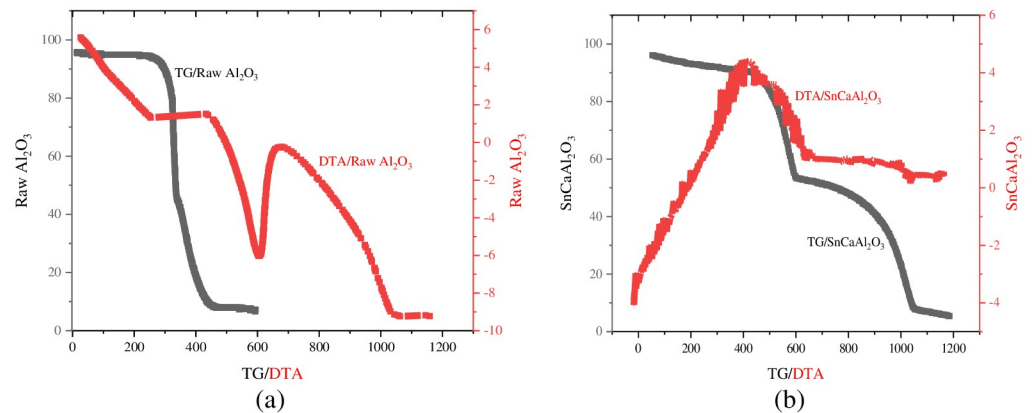


Fig 2. TG/DTA of (a) Al₂O₃, and (b) SnCaAl₂O₃ nanoparticles.

<https://doi.org/10.1371/journal.pone.0276888.g002>

amorphous aluminum hydroxide dehydration [48]. Whereas there is no considerable weight loss after 600°C, the material is thermally stable. As a result, the sorbent material was calcined and obtained alumina particles phase at this temperature.

3.1.3. XRD spectroscopy. XRD examination validated the chemical structure and acquired phase of the as-synthesized nanoparticles. The crystallite size of the as-synthesized materials can be determined using the Scherrer formula (2) and the resultant diffraction peaks [13], in addition to phase confirmation [14]. Fig 3 illustrates the X-ray diffractogram of the formed samples, indicating the creation of the Al₂O₃ species by the four typical peaks at 2θ of 32°, 37.4°, 45.2°, and 67.5° with comparable reflection planes of 220, 311, 400, and 440. The obtained peaks were nicely matched to the database of standards (JCPDS card 00-029-0063).

$$D = 0.9 \frac{\lambda}{FWHM} \cos \theta \quad (2)$$

Whereas D is the crystallite size in nm, λ (0.154056 nm for CuK α radiation) is the wavelength of the monochromatic X-ray beam, $FWHM$ is the full width (rad) for the diffraction peak at half-maximum under consideration, and θ is the Bragg angle (deg) [44, 49, 50]. The average crystallite size of alumina particles was determined at 55 nm after averaging the results from the (2 2 0), (3 1 1), (4 0 0), and (4 4 0) reflections [51, 52]. On the other hand, XRD results point to the creation of SnCaAl₂O₃, which has been found in prior investigations in ceramic compounds, such as a combination of Al₂O₃ and CaCO₃, with a formation temperature of around 1100°C. CaAl₂O₄ was produced at a lower temperature of 250°C in our experiment than previously reported. They discovered that when the CaAl₂O₄ phase is synthesized from ceramic components (Al₂O₃ and CaCO₃) at high temperatures, it coexists with Ca₁₂Al₁₄O₃₃. However, due to lower temperatures or considerably different beginning circumstances, we could not detect the creation of Ca₁₂Al₁₄O₃₃ in our work. Furthermore, other thermodynamically stable phases, such as CaAl₁₂O₁₉, Ca₃Al₂O₆, and Ca₁₂Al₁₄O₃₃, could occur in the Al₂O₃ and CaO system after sintering have not been detected. On the other hand, XRD indicates the production of CaAl₂O₄ [24, 44, 45].

3.1.4. Microstructure of prepared nanoparticles. The morphology and diameter characteristics of the as-prepared nanoparticles can be conducted by HR-TEM analysis. Fig 4 depicts the T.E.M. images of Al₂O₃ nanoparticles with different hexagonal, cylindrical, and spherical-like structures with average crystallite diameter in the range of 44–55 nm, consistent with those obtained from the XRD analysis [53–55]. For further investigation of the micrograph of

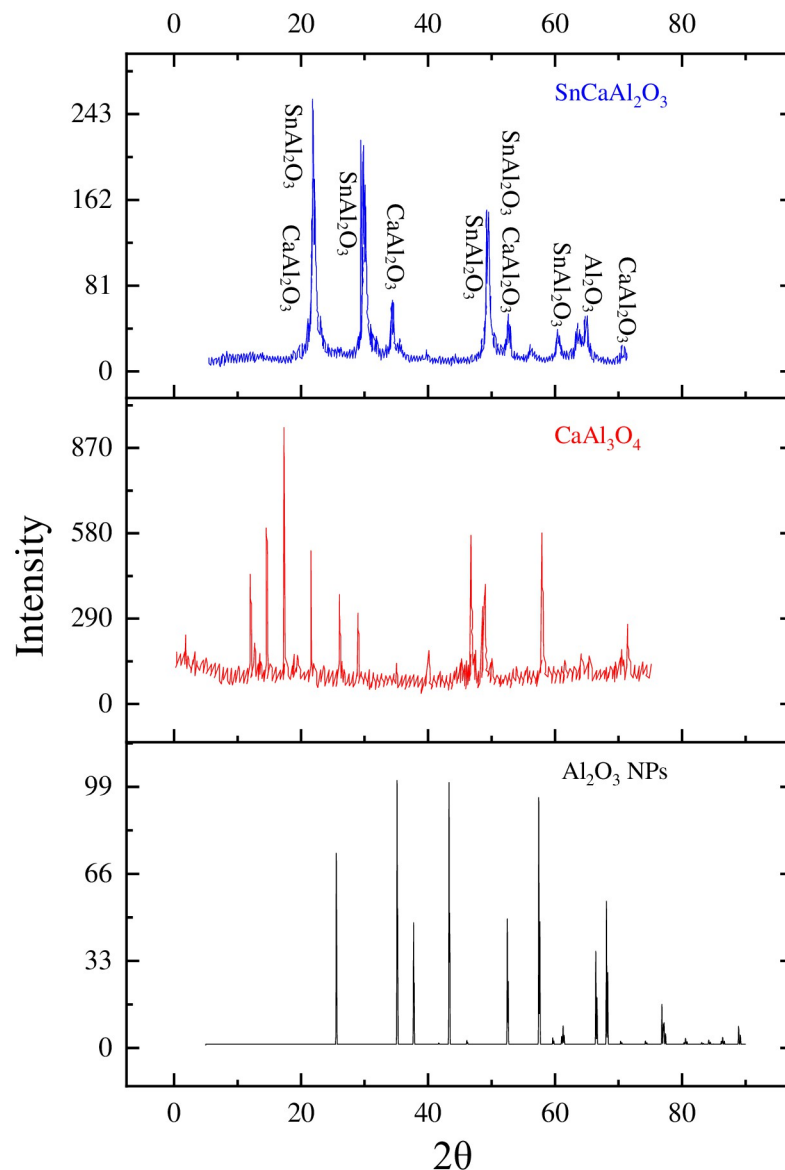


Fig 3. XRD diffraction patterns of Al₂O₃ and SnCaAl₂O₃ nanoparticles.

<https://doi.org/10.1371/journal.pone.0276888.g003>

SnCaAl₂O₃ C.N.P.s. It shows a bulk agglomerate structure composed of thin layers of Al₂O₃ nanoparticles with a Ca-containing layer at the Al₂O₃ interface. This complicated structure is indexed to the monocalcium aluminate SnCaAl₂O₃ (JCPDS no. 23–1036).

On the other hand, FE-SEM utilizes for exploring the sample's surface morphology and the S.E.M. images depicted in Fig 5. From Fig 5a, the S.E.M. micrograph of the Al₂O₃ shows a separate bulk structure composed of thin layers and cracked Al₂O₃ particles, voids, or holes that can trap Sn and Ca within it. The observed voids could be due to escaping gases during the sample's annealing. Moreover, the surface morphology of the SnCaAl₂O nanoparticles shown in Fig 5b has a soft, smooth pattern and sponge shape. As a result of a weak van der Waal bond formation among the particles, they seem to clump together [56].

3.1.5. Surface area of nanoparticles. The prepared samples' textural and surface area characteristics were studied using the N₂ sorption-desorption technique. The obtained IV

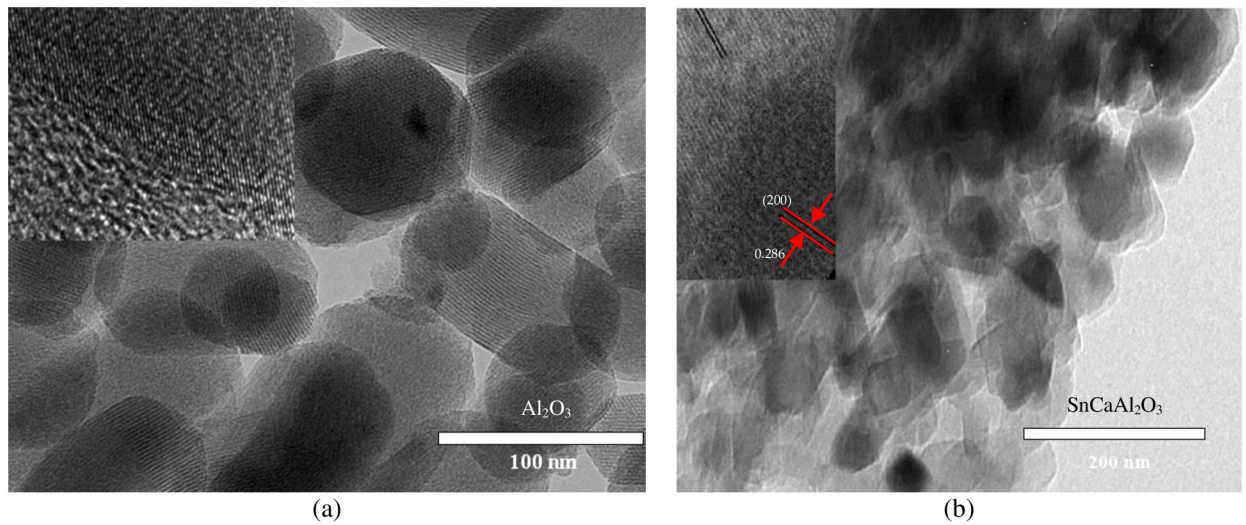


Fig 4. T.E.M. image of Al₂O₃ (a) and SnCaAl₂O₃ (b) nanoparticles.

<https://doi.org/10.1371/journal.pone.0276888.g004>

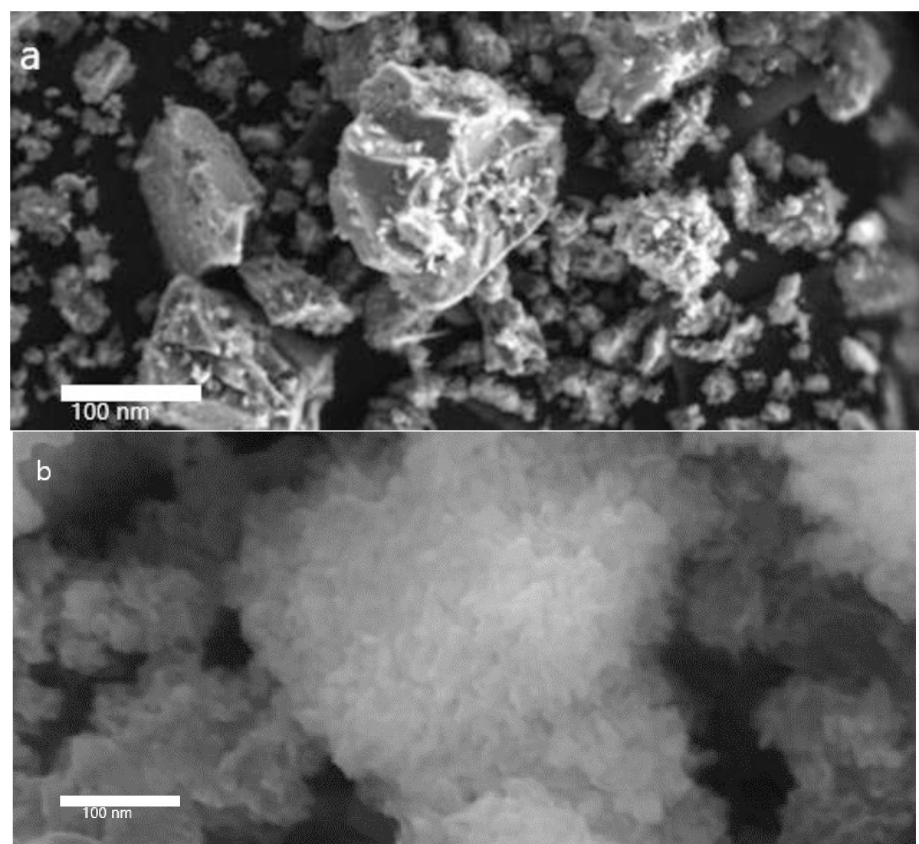


Fig 5. S.E.M. microstructure of Al₂O₃ (a) and SnCaAl₂O₃ nanoparticles (b).

<https://doi.org/10.1371/journal.pone.0276888.g005>

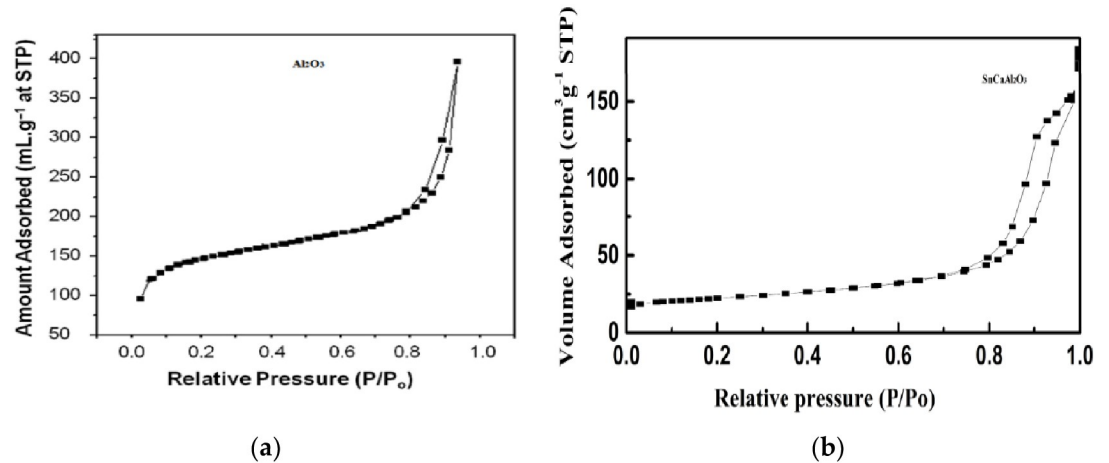


Fig 6. B.E.T. adsorption-desorption isotherm curve for (a) Al₂O₃ and (b) SnCaAl₂O₃.

<https://doi.org/10.1371/journal.pone.0276888.g006>

isotherm with hysteresis type H1 loop indicates a mesoporous structure [57]. Additionally, the Equation of Brunauer–Emmett–Teller (B.E.T.) [58] was applied to investigate the specific surface area, and it was 108 and 390 m²/g SnCaAl₂O₃ and Al₂O₃, respectively (Fig 6). The calculated specific surface area was greater than 344 m²/g, confirming the creation of thermodynamically stable alumina. The B.J.H. pore size distribution curves were analyzed to determine the pore size of the studied samples [59]. As shown in Fig 7, about 90% of the pores were in the range of 2–50 nm, indicating the mesoporous nature of the adsorbent, while the rest (10%) of the pores were below 2 nm, representing the microporous character. The pore

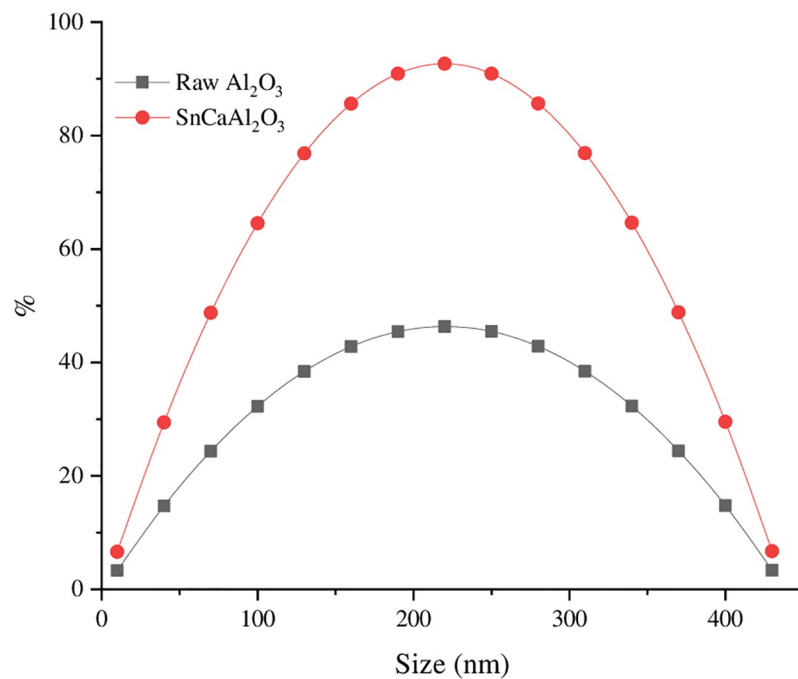


Fig 7. Particle size distribution of Al₂O₃ and SnCaAl₂O₃ NPs.

<https://doi.org/10.1371/journal.pone.0276888.g007>

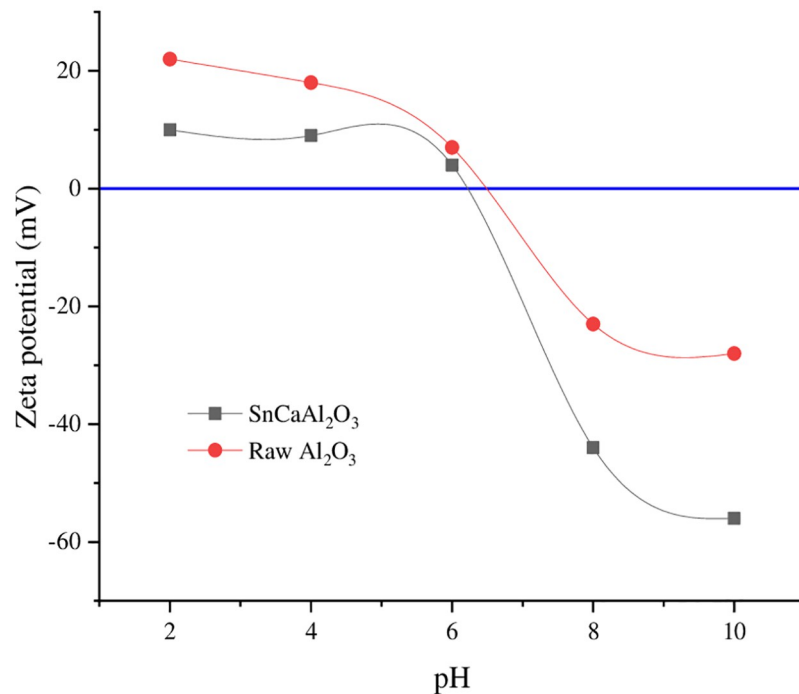


Fig 8. Zeta potential of Al₂O₃ and SnCaAl₂O₃ nanoparticles.

<https://doi.org/10.1371/journal.pone.0276888.g008>

size and volume of the adsorbent were calculated as 13.6 nm and 0.32 cm³/g, respectively. As a result, mesoporous structures and a large pore volume provide a suitable adsorptive environment for eliminating Zn⁺², Cd⁺², and Pb⁺² ions.

3.1.6. Zeta optional of the prepared nanoparticles. The pH of the zero-point charge (pH_{ZPC}) is the point at which the surface of the substance is electrically neutral (zero charges), whereas, beneath this point, the material surface is positively charged. In contrast, above this point, it is negatively charged. Knowing the pH of the pH_{ZPC} gives reasonable expectations about the manner of the adsorption process and at which favorable pH range. From Fig 8, the pH_{ZPC} of alumina nanoparticles was 6.4, close to that reported by many authors [60, 61]. The pH_{ZPC} of SnCa is 6.2, indicating the pH_{ZPC} to a lower value due to the defect of oxygen atoms in the composite crystals that make the charge move in a positive direction more than a negative one. In addition, at relatively high N.P.s concentrations, which leads to the particle's aggregation and the effective surface charge on N.P.s decreases, the repulsion between the N.P.s decreases.

3.2. Adsorption parameters of heavy metals on SnCaAl₂O₃ nanoparticles

3.2.1. pH Effect. The pH determines the sorption behavior of a solution and whether it will occur in an acidic or alkaline medium. This effect can result in the surface charge of both adsorbent and adsorbate species [26, 60]. Accordingly, the role of solution pH in removing Zn⁺², Cd⁺², and Pb⁺² by SnCaAl₂O₃ nanoparticles was carried out by pH varying from 2 to 9 at room temperature with an initial Zn⁺², Cd⁺², and Pb⁺² concentration of 500 mg/L. Fig 9 shows that the removal efficiency of Zn⁺², Cd⁺², and Pb⁺² increases gradually from pH 2 until reaching its maximum at pH 7, with the highest removal percent of 84.4%, 87%, and 84.8% for the ions of Zn, Pb, and Cd, respectively. Further increasing the solution pH above 8 may

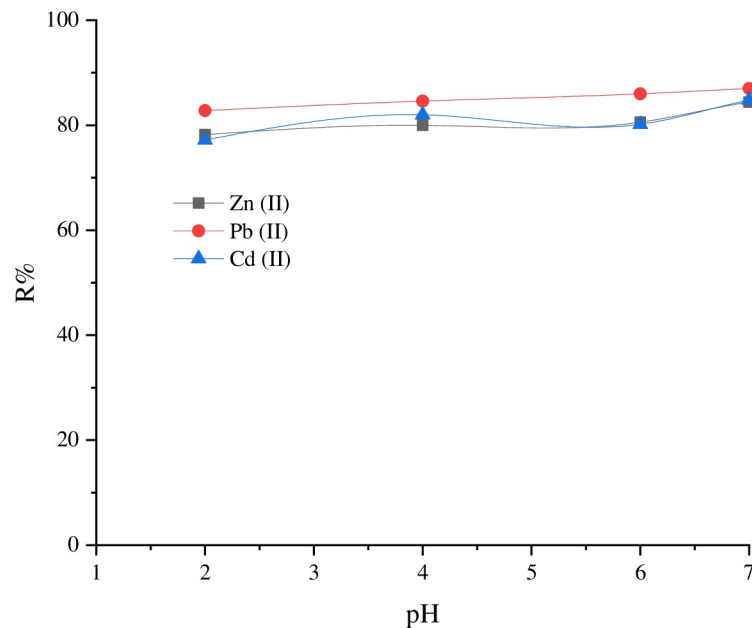


Fig 9. The pH effect on the SnCaAl₂O₃ nanoparticles' adsorption of Zn⁺², Cd⁺², and Pb⁺², at constant adsorbent dose, initial concentration of ions, contact time, and volume of polluted water.

<https://doi.org/10.1371/journal.pone.0276888.g009>

indicate a higher removal percent due to precipitation of the hydroxide form of Zn⁺², Cd⁺², and Pb⁺² ions [62]. The mechanism of the removal process may be explained depending on the surface chemistry of the adsorbent SnCaAl₂O₃ nanoparticles, where the metal oxide surfaces in an aqueous phase behave amphotericly and respond to pH changes by undergoing acid-base interactions in the aqueous phase [63, 64].

3.2.2. Adsorbent dosage effect. The SnCaAl₂O₃ adsorbent dosage effect on Zn⁺², Cd⁺², and Pb⁺² removal via adding various weights ranging from 0.02 up to 1 g to 50 mL (aqueous solution) of 500 mg/L Zn⁺², Cd⁺², and Pb⁺² as an initial concentration, was investigated. Fig 10 illustrates that the removal percent increases with adsorbent doses from 0.02 to 0.5 g. This may attribute to the superior surface-active sites readily available for adsorption of the pollutant's ions [64]. In addition, further increasing with the added weight of the adsorbent did not result in much increase in the removal percent. In other words, a high dose of the adsorbent may result in agglomeration in the solution, decreasing the removal percent [65–68]. Therefore, the optimum adsorbent dose is 0.5 g.

3.2.3. Contact time Vs. sorption kinetics. The effect of contact time on the SnCaAl₂O₃ nanoadsorbent removal efficiency was examined at pH 8, using a known weight of the adsorbent with a constant high concentration (500 mg/L) of Zn⁺², Cd⁺², and Pb⁺². Fig 11 represents the removal percent against the stirring time between 10 and 80 min. It is recognized that as the contact period grew until 30 min, sorption increased. Then, it reached equilibrium [69]. The equilibrium time needed for SnCaAl₂O₃ NPs interactions with all initial Zn⁺², Cd⁺², and Pb⁺² concentrations in a steady state is 30 min. It indicates that the interaction is concentration-independent. The fast removal of the studied ions within 30 min may interrelate to the adsorbent surface free-active sites for attracting the pollutants ions from the aqueous solution [70]. Further increasing the interaction time, the removal rate decreases slowly. The adsorption curves show almost straight lines corresponding to the full coverage and saturation of the adsorbent surface-active sites (Fig 11C).

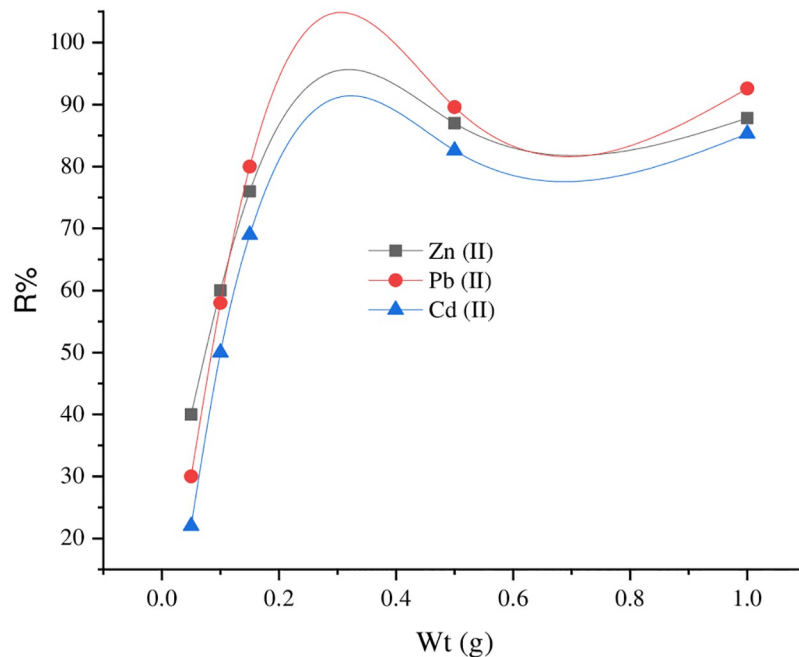


Fig 10. The SnCaAl₂O₃ nanoparticles dose effect on the adsorptions of Zn⁺², Cd⁺², and Pb⁺², at the constant of volume solution (50 ml) and initial concentration of these ions (500 mg/l).

<https://doi.org/10.1371/journal.pone.0276888.g010>

3.3. Adsorption kinetics and isotherm models

3.3.1. Kinetics models. The heavy metals sorption mechanism was studied using SnCaAl₂O₃ nanoparticles, and kinetics models were used to examine the experimental data obtained in the study. Pseudo-first-order and pseudo-second-order kinetic models were used. Adsorption kinetic parameters were studied for contact times varied from 5 to 200 min via monitoring the adsorption capacity of Zn⁺², Pb⁺², and Cd⁺² by the adsorbent through this time interval.

Pseudo-First-Order Kinetics (Lagergren)

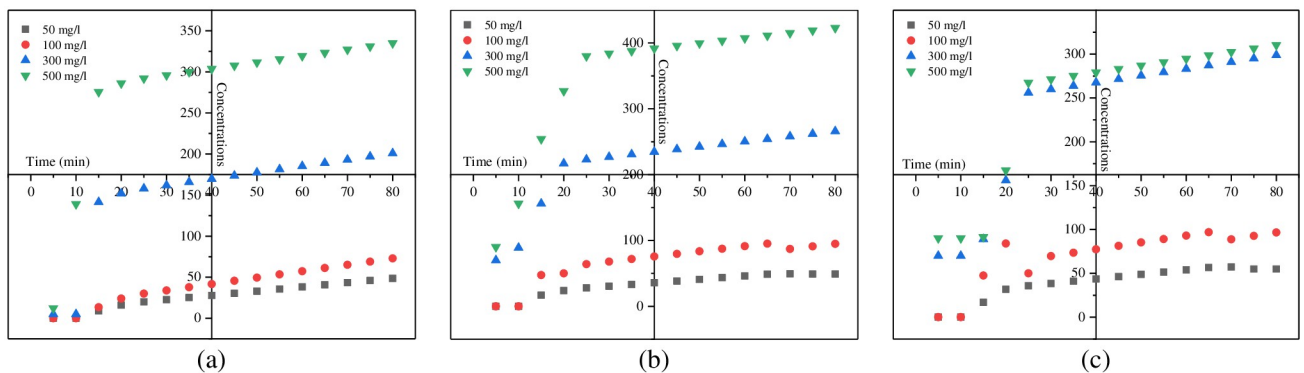


Fig 11. Influence of contact time on adsorption of (a) Zn⁺², (b) Pb⁺², and (c) Cd⁺² in SnCaAl₂O₃ NPs at constant adsorbent dose, initial concentration of ions, and volume of polluted water.

<https://doi.org/10.1371/journal.pone.0276888.g011>

Table 1. The pseudo-first-order and pseudo-second-order kinetic parameters for sorption of Zn⁺², Pb⁺², and Cd⁺² using SnCaAl₂O₃ nanoadsorbent.

Pseudo Order	Ions		
	Zn(II)	Pb(II)	Cd(II)
Kinetics Model of Pseudo-First-Order			
Q _e , mg/g	46.27510	35.38621	40.32178
K ₁	-0.0096	-0.02261	-0.02735
R ²	0.933421	0.891272	0.922456
Kinetics Model of Pseudo-Second-Order			
Q _e , mg/g	50	40.87709	43.48520
K ₂	0.134156	0.180427	0.278443
R ²	0.995548	0.993413	0.994842

<https://doi.org/10.1371/journal.pone.0276888.t001>

Eq (3) gives the linear form:

$$\log(q_e - qt) = \log(q_e) - K_1 2.303t \quad (3)$$

Table 1 reveals the parameters of the Lagergren model created from the experimental kinetic data. The straight-line emerges through plotting $\log(q_e - qt)$ against t . Although, K_1 and the theoretical q_e may be derived from slope and intercept (S1 Fig). The plot of $\log(q_e - qt)$ illustrates the respective estimated value against the corresponding equilibration time t in hours.

Eq (4) describes Pseudo-second-order model [71, 72].

$$t_{qt} = 1K_2q_e^2 + t_{q_e} \quad (4)$$

Whereas q_e and q_t are the amount of metal ions adsorbed at equilibrium time and instant time (t). K_1 = adsorption rate constant (g/mg min) and K_2 = pseudo-second-order reaction rate constant (g/mg min). The graphs of kinetic models for Zn⁺², Pb⁺², and Cd⁺² adsorption using SnCaAl₂O₃ nanoadsorbent are stated in (S1 Fig).

Table 1 reveals that the sorption data fit was consistent with the pseudo-second-order model by a strong correlation coefficient R^2 and is near 1 for Zn⁺², Pb⁺², and Cd⁺². Furthermore, the pseudo-second-order model's $Q_{e,cal}$ (calculated) value is very equivalent to the $Q_{e,exp}$ (experimental), which is considered after Eq (2) through a correlation coefficient greater than the pseudo-first-order. These results suggested the involvement of chemisorption in Zn⁺², Pb⁺², and Cd⁺². Chemisorption synchronization arises once a chemical bonding originates between metals and adsorbent surface that increases with active sites.

3.3.2. Isotherm models. Table 2 reveals that the isotherm of SnCaAl₂O₃ nanoparticle's multilayer adsorption was acceptable for the Freundlich model. The q_e fitted value via the Langmuir model differs from the current data. Cations are built through cross whiskers and the surface of whiskers and may accumulate in the SnCaAl₂O₃ NPs pores [64, 65]. The cation exchange and surface adsorption process may describe the adsorption mechanism. Therefore, the adsorption of the heavy metals on SnCaAl₂O₃ nanoparticles may comprise both single layer chemical adsorption and multilayer physical adsorption. Hence, the features of isotherms display multilayer physical adsorption (S2 Fig).

3.3.3. Heavy metals concentration Vs. adsorption equilibrium. The adsorption capacity of the as-synthesized SnCaAl₂O₃ nanoparticles was investigated at pH = 8 with different concentrations of Zn⁺², Pb⁺², and Cd⁺² in the range of 50 to 500 mg/L, with 30 min stirring time at 25°C. Fig 12 revealed that the removal efficiency increased at low initial pollutants concentration and decreased gradually with increasing the concentration at 500 mg/L. This is related

Table 2. Constants of Langmuir, Freundlich, isotherm.

Langmuir		Freundlich	
Pb			
b	0.020293	K _f	1.393201
R ²	0.991001	1/n	0.530594
R _L	0.985558	R ²	0.961846
q _{max}	36.61836	-	-
Cd			
b	0.013614	K _f	1.01943
R ²	0.995437	1/n	0.992335
R _L	1.469115	R ²	0.999525
q _{max}	40.00987	-	-
Zn			
b	0.011401	K _f	1
R ²	0.929377	1/n	1
R _L	1.754287	R ²	1
q _{max}	34.60915	-	-

<https://doi.org/10.1371/journal.pone.0276888.t002>

to the adsorbent free active site's saturation. In comparison, the adsorption capacity of the adsorbent increased in higher initial concentrations of the pollutants because the driving force increased, which increased the interactions between metal ions and the active adsorbent sites [71, 73, 74]. Fig 12 reveals that the adsorption capacity Q_e displays a reverse relationship to the initial concentration C_0 . In contrast, metal ions have a strong negative correlation as the initial concentration C_0 increases.

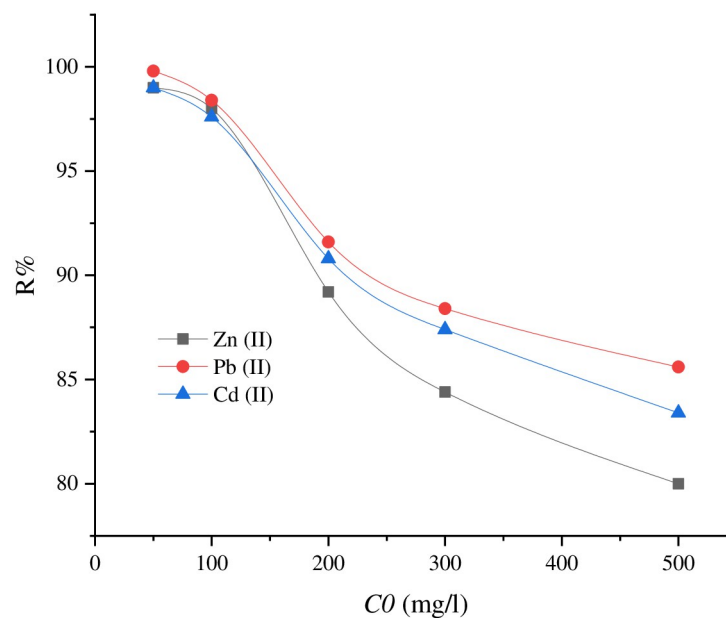


Fig 12. Adsorption capacities of SnCaAl₂O₃ nanoparticles as a function of Zn⁺², Pb⁺², and Cd⁺² ions concentration at constant adsorbent dose, contact time, and volume of polluted water.

<https://doi.org/10.1371/journal.pone.0276888.g012>

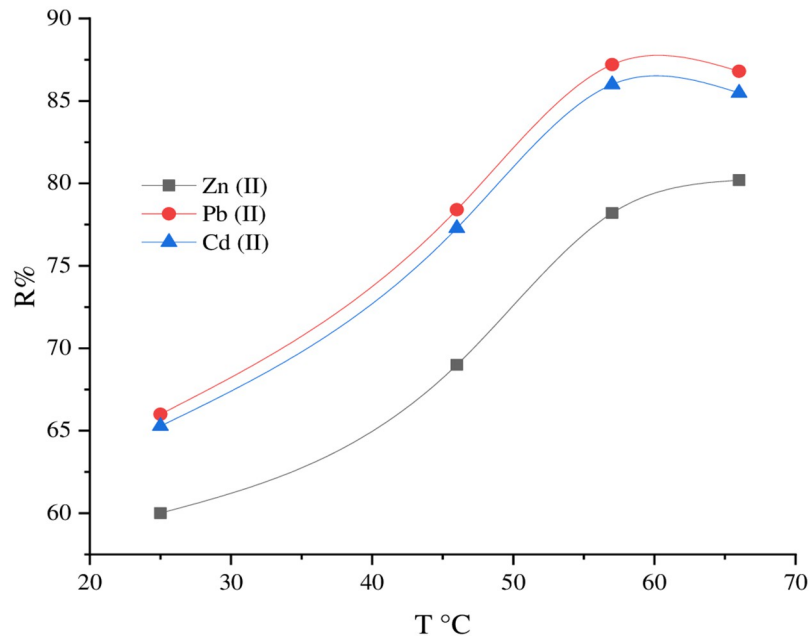


Fig 13. The Zn⁺², Pb⁺², and Cd⁺² adsorption by the SnCaAl₂O₃ nanoparticles under various temperatures (25–66°C), at constant adsorbent dose, contact time, optimum pH, initial concentration of ions, and volume of polluted water.

<https://doi.org/10.1371/journal.pone.0276888.g013>

3.3.4. The role of temperature on the adsorption rate of metal ions. The effect of the adsorption rate of Zn⁺², Pb⁺², and Cd⁺² by the SnCaAl₂O₃ nanoparticles was considered by mixing 1 g of SnCaAl₂O₃ with 15 mL of metal ions solution with a concentration of 500 mg/L accompanied by shaking for 30 min in a temperature range of 25–66°C. Fig 15 displays that the removal efficacy of the pollutants increased with the temperature increase, which confirms the endothermic nature of the adsorption method. This behavior may result from the increase in the speed or the mobility of the pollutants in the solution toward the active adsorbent sites [75, 76]. As shown in Fig 13, the adsorption capacity (Q_e) is proportional directly to the elevated temperature.

3.4. Thermodynamics study

Thermodynamic parameters ΔG (Standard Gibbs free energy), ΔH (standard enthalpy), and ΔS (standard entropy) are considered for Zn⁺², Pb⁺², and Cd⁺² adsorption onto SnCaAl₂O₃ nanoparticles, the Eqs (5–7) calculate ΔG, ΔH, and ΔS [69]:

$$\Delta G^{\circ} = RT \ln K'_{L} \quad (5)$$

$$\ln \frac{K_{L2}}{K_{L1}} = - \left(\frac{\Delta H^{\circ}}{R} \right) \left(\frac{T1 - T2}{T_1 T_2} \right) \quad (6)$$

$$\Delta S^{\circ} = \frac{\Delta H^{\circ} - \Delta G^{\circ}}{T} \quad (7)$$

The Langmuir constants are K_{L1} and K_{L2} at T₁ and T₂, respectively. As well as, R is the gas constant (8.314 J mol⁻¹ K⁻¹).

Table 3. ΔH , ΔS , and ΔG for Zn⁺², Pb⁺², and Cd⁺² adsorption on the SnCaAl₂O₃ nanoparticles.

Pb			
T (K)	H (J/mol)	S (J/mol K)	G (J/mol)
298.15	-15448	58.73833	-32960.8
313.15			-2288.52
333.15			-5746.57
353.15			-4480.29
Cd			
T (K)	H (J/mol)	S (J/mol K)	G (J/mol)
298.15	-11575.4	50.04279	-26495.7
313.15			-28503.1
333.15			-31995.8
353.15			-31988.9
Zn			
T (K)	H (J/mol)	S (J/mol K)	G (J/mol)
298.15	-7924.8	41.09136	-20176.2
313.15			-22078.1
333.15			-22899.9
353.15			-23721.8

<https://doi.org/10.1371/journal.pone.0276888.t003>

Table 3 shows the thermodynamic parameters of Zn⁺², Pb⁺², and Cd⁺² adsorption onto SnCaAl₂O₃ nanoparticles at varied temperatures. The ΔH and ΔS changes were calculated as the slope and intercept of the linear plot $\ln K_c$ against $1/T$ (S3 Fig) [77]. From the Van't Hoff equation ΔH , ΔS , and ΔG are calculated using Eqs (5), (6) and (7). The negative values were revealing of a spontaneous adsorption process as temperature increases. The positive values refer to the affinity of the SnCaAl₂O₃ nanoparticles for Zn⁺², Pb⁺², and Cd⁺². Therefore, chemical and physical adsorption may occur simultaneously [70]. The adsorption heat for van Edward force is in the range of 4–10, the hydrogen bond between 2–40, ligand exchange is 40, dipole interaction ranges from 2–29, and the chemical bond is $>60 \text{ kJ mol}^{-1}$ [63]. In the current finding, the values are in a similar range, representing the adsorption through the hydrogen bond besides ligand exchange. Thus, physical and chemical adsorption contributed to Zn⁺², Pb⁺², and Cd⁺² adsorption onto SnCaAl₂O₃ nanoparticles.

3.5. Effect of coexisting ions

Many inorganic anions and cations are present in wastewater discharged. Therefore, it is critical to test the adsorbent's selectivity for certain ions in the occurrence of competing ions. Adsorption effectiveness of SnCaAl₂O₃ nanoparticles for Zn⁺², Pb⁺², and Cd⁺² ions in coexisting ions such as Na⁺ and Ca²⁺ was investigated. Fig 14 demonstrates that the coexistence of Na⁺ and Ca²⁺ ions did not affect the removal efficiency of Zn⁺², Pb⁺², and Cd⁺² from SnCaAl₂O₃ nanoparticles. The strong affinity of SnCaAl₂O₃ nanoparticles for Zn⁺², Pb⁺², and Cd⁺² may explain via the development of the surface of the outer-sphere complexes on metal hydroxides [78]. When SnCaAl₂O₃ nanoparticles utilize as adsorbents, Na⁺ and Ca²⁺ ions in an aqueous solution are not a limiting factor in the treatment process.

3.6. Regeneration and desorption

The reusability of SnCaAl₂O₃ nanoparticles adsorbent for wastewater treatment and removal of the pollutants from the aqueous medium is of great economic value. This property can be

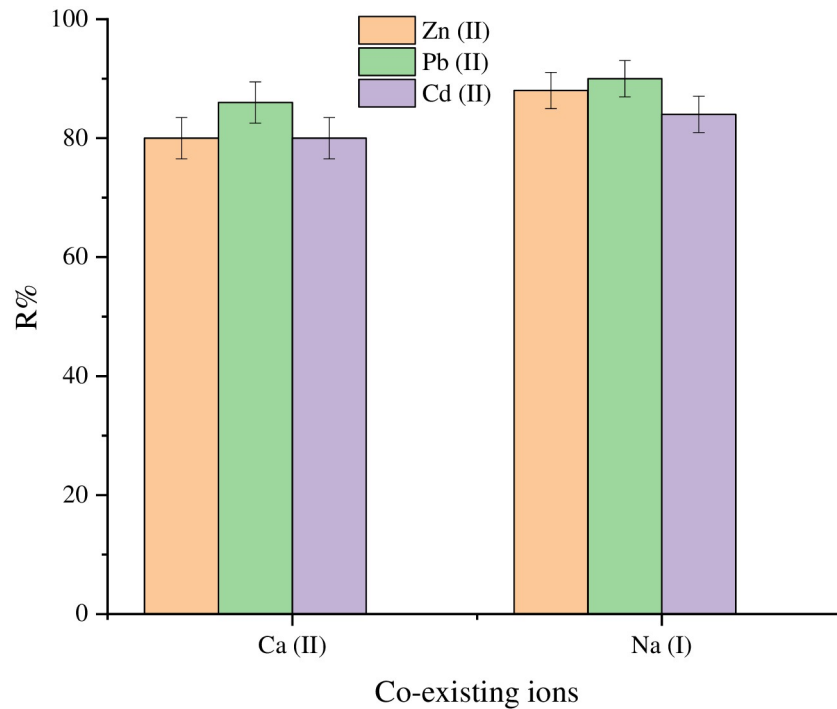


Fig 14. Coexisting Na⁺ and Ca²⁺ affect Zn²⁺, Pb²⁺, and Cd²⁺ uptake by SnCaAl₂O₃ nanoparticles.

<https://doi.org/10.1371/journal.pone.0276888.g014>

studied by regeneration of the SnCaAl₂O₃ nanoadsorbent using 30 mL of HCl 0.5 mol L⁻¹ and 30 mL of NaOH 0.5 mol L⁻¹. The desorption of Zn²⁺, Pb²⁺, and Cd²⁺ can attain via controlling the solution pH. Therefore, NaOH and HCl solutions can regenerate the active adsorbent sites. Therefore, recovery of the adsorption properties of the adsorbent would be achieved [79]. As a result of using the abovementioned concentrations of HCl and NaOH, the desorption efficiencies for Zn²⁺, Pb²⁺, and Cd²⁺ loaded on SnCaAl₂O₃ nanoadsorbent reached around 100% [80]. This proves that the as-synthesized SnCaAl₂O₃ nanoadsorbent has suitable adsorption-desorption properties for removing Zn²⁺, Pb²⁺, and Cd²⁺ [81]. As depicted in Fig 15, the adsorption studies were applied with five cycles. The removal efficiencies decreased to 92% and 94% after the third cycle and 90% and 88% after the fifth cycle for Zn²⁺, Pb²⁺, and Cd²⁺ ions, respectively.

4. Adsorption mechanism of Zn²⁺, Pb²⁺, and Cd²⁺ by SnCaAl₂O₃ NPs

Adsorption consists of three main steps: (1) film diffusion; where the motion of the bulk liquid adsorbate is surrounded by a film of the adsorbent, (2) surface adsorption; whereas the adsorbate transport from the film to the surface of the adsorbent, and (3) intraparticle diffusion; the adsorbate transmission to the internal active sites which attach to the heavy metal ions [70].

The slowest step of adsorption (limiting step) is the process that controls the whole adsorption rate. Performed by several kinetic models are applied to examine the rate-limiting step; this includes P.F.O. and PSO. At the same time, the adsorption process is chemisorption's, and the adsorption percentage increase due to the interaction of Zn²⁺, Pb²⁺, and Cd²⁺ ions with the surface functional groups of the adsorbents as a result of the ion exchange mechanism or through hydrogen bonding [69].

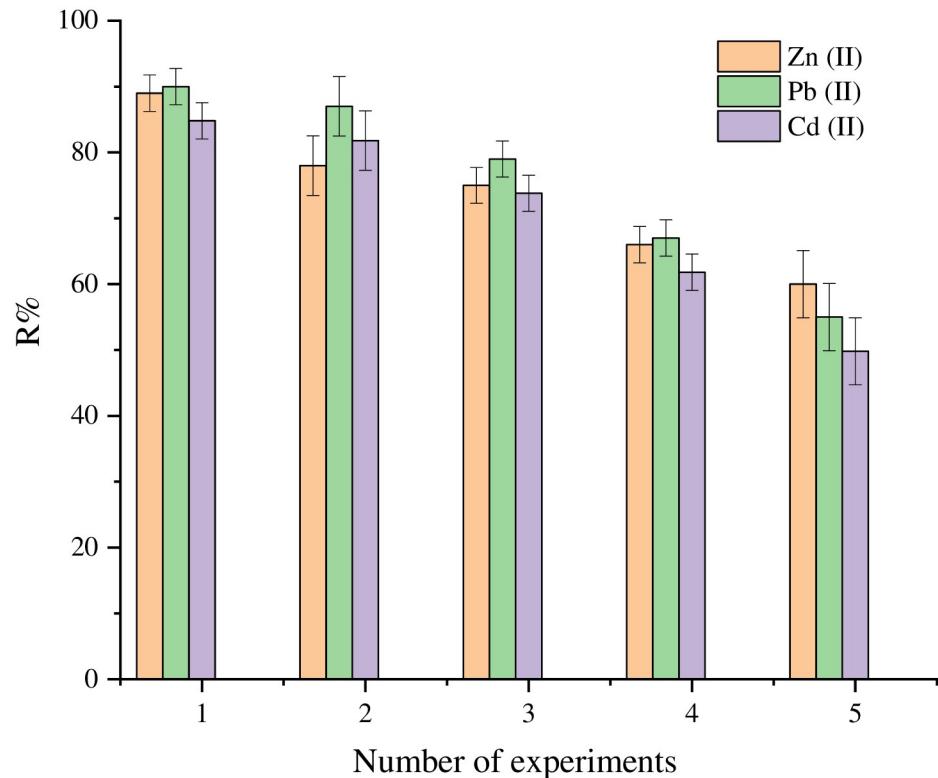


Fig 15. Desorption of Zn²⁺, Pb²⁺, and Cd²⁺ and regeneration process of SnCaAl₂O₃ nanoparticles.

<https://doi.org/10.1371/journal.pone.0276888.g015>

5. Evaluation of the SnCaAl₂O₃ adsorption capacity

Table 4 compares q_{\max} values with various adsorbents of Zn²⁺, Pb²⁺, and Cd²⁺, the SnCaAl₂O₃ nanoparticles existing advanced adsorption capacity. On the other hand, SnCaAl₂O₃ nanoparticles have a reasonable material cost and economic benefit as promising materials for alleviating Zn²⁺, Pb²⁺, and Cd²⁺.

6. Conclusions

The present study focused on synthesizing and characterizing a novel SnCaAl₂O₃ nanoadsorbent of crystallite size of a diameter of 55 nm to use it as a superior adsorbent material to remove the Zn²⁺, Pb²⁺, and Cd²⁺ from polluted water. The maximum removal efficiency was achieved at pH 8, with an equilibrium time of 30 min using 1 g of the adsorbent. Afterward, the adsorption kinetics were examined via P.F.O. and PSO models; PSO gives the best fit for all adsorbents. In addition, the adsorption isotherms were considered at equilibrium. The Freundlich isotherm model clarifies the adsorption of Zn²⁺, Pb²⁺, and Cd²⁺ by the SnCaAl₂O₃ nanoadsorbent. The thermodynamic studies prove that Zn²⁺, Pb²⁺, and Cd²⁺ adsorption onto SnCaAl₂O₃ nanoadsorbent is exothermic and spontaneous. SnCaAl₂O₃ nanoadsorbent was recycled to remove the concerned adsorbent for five cycles, with high adsorption efficiency ranging from 88% to about 100%, and after the fifth regeneration cycle, adsorption efficiency reached about 88%. SnCaAl₂O₃ nanoadsorbent exhibited suitable selective adsorption for Zn²⁺, Pb²⁺, and Cd²⁺ even in the presence of Na⁺ and/or Ca²⁺ competing cations. The

Table 4. The comparison of maximum adsorption capacity of Zn⁺², Pb⁺², and Cd⁺² on various adsorbents at neutral pH (6.5–8.5).

Adsorbent	Metal ⁺²	q _{max} (mg/g)	Ref.
Soy protein	Zn	39.780	[82]
	Cd	10.914	
	Pb	11.526	
Chitosan polyitaconic acid	Cd	36.720	[83]
	Pb	16.422	
Calcium alginate	Pb	5.304	[84]
	Cd	8.160	
Succinylated starch	Zn	0.204	[85]
	Cd	7.548	
Dibenzo-18-crown-grafted corn starch	Zn	5.712	[86]
	Cd	2.142	
Cross-linked starch phosphate carbamate cross-linked starch phosphate	Pb	2.040	[87]
	Zn	1.122	
	Pb	58.854	
	Pb	33.354	
SnCaAl ₂ O ₃ nanoparticles	Zn	290	this study
	Pb	345	this study
	Cd	382	this study

<https://doi.org/10.1371/journal.pone.0276888.t004>

prepared SnCaAl₂O₃ nanoadsorbent attributes make it a promising, low-cost, efficient adsorbent for treating wastewater.

Supporting information

S1 Fig. Adsorption kinetics of (a,b) Zn⁺², (c,d) Pb⁺², and (e,f) Cd⁺² adsorption on SnCaAl₂O₃ nanoadsorbent.

(DOCX)

S2 Fig. Adsorption isotherm for (a,b) Zn⁺², (c,d) Pb⁺², and (e,f) Cd⁺² ions.

(DOCX)

S3 Fig. The linear plot lnK_c versus 1/T for (a) Zn⁺², (b) Pb⁺², and (c) Cd⁺² adsorption on the SnCaAl₂O₃ nanoparticles.

(DOCX)

Author Contributions

Conceptualization: Moustafa Gamal Snousy, Mahmoud F. Mubarak, Ahmed H. Ragab, Atef Mohamed Gad Mohamed, Abeer El Shahawy.

Data curation: Ali Sayqal, Moustafa Gamal Snousy, Mahmoud F. Mubarak, Atef Mohamed Gad Mohamed.

Formal analysis: Moustafa Gamal Snousy, Mahmoud F. Mubarak, Ahmed H. Ragab.

Funding acquisition: Ali Sayqal, Ahmed H. Ragab.

Investigation: Ali Sayqal, Moustafa Gamal Snousy, Mahmoud F. Mubarak, Atef Mohamed Gad Mohamed, Abeer El Shahawy.

Methodology: Atef Mohamed Gad Mohamed, Abeer El Shahawy.

Supervision: Abeer El Shahawy.

Writing – original draft: Ali Sayqal, Moustafa Gamal Snousy, Mahmoud F. Mubarak, Ahmed H. Ragab, Atef Mohamed Gad Mohamed, Abeer El Shahawy.

Writing – review & editing: Moustafa Gamal Snousy, Atef Mohamed Gad Mohamed, Abeer El Shahawy.

References

1. Farrag A.E.H., Moghny TA., Mohamed A.M.G., Saleem SS, Fathy M (2017), Abu Zenima synthetic zeolite for removing iron and manganese from Assiut governorate groundwater. *Egypt. Applied Water Science* 7 (6): 3087–3094.
2. Fathy M, Zayed M A, Mohamed A M G. (2019), Phosphate adsorption from aqueous solutions using novel Zn Fe/Si MCM 41 magnetic nanocomposite: characterization and adsorption studies. *Nanotechnology for Environmental Engineering* 4:14 <https://doi.org/10.1007/s41204-019-0061-7>
3. Naushad M., Sharma G., & Alothman Z. A. (2019). Photodegradation of toxic dye using Gum Arabic-crosslinked-poly (acrylamide)/Ni (O.H.) 2/FeOOH nanocomposites hydrogel. *Journal of Cleaner Production*, 241, 118263.
4. Ali I., Alharbi O. M., AlOthman Z. A., Al-Mohaimed A. M., & Alwarthan A. (2019). Modeling of fenuron pesticide adsorption on C.N.T.s for mechanistic insight and removal in water. *Environmental research*, 170, 389–397.
5. Al-Janabi A.; Malayeri M.R.; Badran O.O. Performance of shot-peened surfaces subject to crystallization fouling. *Int. J. Therm. Sci.* 2017, 111, 379–389.
6. Ali E.S.; Alsaman A.S.; Harby K.; Askalany A.A.; Diab M.R.; Yakoot S.M. Recycling brine water of reverse osmosis desalination employing adsorption desalination: A theoretical simulation. *Desalination* 2017, 408, 13–24.
7. Wabaidur S. M., Khan M. A., Siddiqui M. R., Otero M., Jeon B. H., Alothman Z. A., et al. (2020). Oxygenated functionalities enriched MWCNTs decorated with silica coated spinel ferrite—A nanocomposite for potentially rapid and efficient de-colorization of aquatic environment. *Journal of Molecular Liquids*, 317, 113916.
8. Kenawy E. R., Ghfar A. A., Wabaidur S. M., Khan M. A., Siddiqui M. R., Alothman Z. A., et al. (2018). Cetyltrimethylammonium bromide intercalated and branched polyhydroxystyrene functionalized montmorillonite clay to sequester cationic dyes. *Journal of Environmental Management*, 219, 285–293. <https://doi.org/10.1016/j.jenvman.2018.04.121> PMID: 29751259
9. Aftab B.; Khan S.J.; Maqbool T.; Hankins N.P. Heavy metals removal by osmotic membrane bioreactor (OMBR) and their effect on sludge properties. *Desalination* 2017, 403, 117–27.
10. Mahmoud EA, Mohamed A.M.G., El Hay A, Farrag A, Aboeldahb S.A.M. (2021), Evaluation of the most promising techniques overcoming the algal problems takes place during the purification of drinking water. *Environ Sci Pollut Res.*, Springer-Nature. <https://doi.org/10.1007/s11356-021-13674-3> PMID: 33846925
11. Bader B.; Aissaoui F.; Krmicha I.; Salem A.B.; Chehab H.; Gargouri K.; et al. Effects of salinity stress on water desalination, olive tree (*Olea europaea* L. cvs 'Picholine', 'Meski' and 'Ascolana') growth and ion accumulation. *Desalination* 2015, 364, 46–52.
12. Bahar R.; Hawlader M.N.A.; Ariff T.F. Channeled coolant plate: A new method to enhance freshwater production from an air gap membrane distillation (AGMD) desalination unit. *Desalination* 2015, 359, 71–81.
13. Poudel M.B.; Ojha G.P.; Kim H.J. Manganese-doped tungsten disulfide microcones as binder-free electrode for high performance asymmetric supercapacitor. *J. Energy Storage* 2022, 47, 103674.
14. Gao Y.; Li G.; Wang F.; Chu J.; Yu P.; Wang B.; et al. A high-performance aqueous rechargeable zinc battery based on organic cathode integrating quinone and pyrazine. *Energy Storage Mater.* 2021, 40, 31–40.
15. Mohamed A.M.G., Mohamed M AM, Farrag AA, Ali A.R.M. (2021), Novel Elimination Method of Iron and Manganese Ions from Drinkable Groundwater in Assiut, Egypt by Using Sodalite Bearing Modified Illite *Environ Sci Pollut Res.*, Springer-Nature. <https://doi.org/10.1007/s11356-021-17765-z> PMID: 34860344

16. Poudel M.B.; Kim H.J. Confinement of Zn-Mg-Al-layered double hydroxide and α -Fe₂O₃ nanorods on hollow porous carbon nanofibers: A free-standing electrode for solid-state symmetric supercapacitors. *Chem. Eng. J.* 2022, 429, 132345.
17. Yi W.; Yang K.; Ye J.; Long Y.; Ke J.; Ou H. Triphenyltin degradation and proteomic response by an engineered *Escherichia coli* expressing cytochrome P450 enzyme. *Ecotoxicol. Environ. Saf.* 2017, 137, 29–34.
18. Yang H.; Elma M.; Wang D.K.; Motuzas J.; da Costa J.C. Interlayer-free hybrid carbon-silica membranes for processing brackish to brine salt solutions by pervaporation. *J. Membr. Sci.* 2017, 523, 197–204.
19. Khan M. A., Alqadami A. A., Wabaidur S. M., Siddiqui M. R., Jeon B. H., Alshareef S. A., et al. (2020). Oil industry waste based non-magnetic and magnetic hydrochar to sequester potentially toxic post-transition metal ions from water. *Journal of Hazardous Materials*, 400, 123247. <https://doi.org/10.1016/j.jhazmat.2020.123247> PMID: 32947690
20. Mittal A., Naushad M., Sharma G., Alothman Z. A., Wabaidur S. M., & Alam M. (2016). Fabrication of MWCNTs/ThO₂ nanocomposite and its adsorption behavior for the removal of Pb (II) metal from aqueous medium. *Desalination and Water Treatment*, 57(46), 21863–21869.
21. Azhar A., Yamauchi Y., Allah A. E., Alothman Z. A., Badjah A. Y., Naushad M., et al. (2019). Nanoporous iron oxide/carbon composites through in-situ deposition of prussian blue nanoparticles on graphene oxide nanosheets and subsequent thermal treatment for supercapacitor applications. *Nanomaterials*, 9 (5), 776. <https://doi.org/10.3390/nano9050776> PMID: 31117195
22. Guo Q., Chen C., Zhou L., Li X., Li Z., Yuan D., et al. (2018). Design of ZIF-8/ion copolymer hierarchically porous material: coordination effect on the adsorption and diffusion for carbon dioxide. *Microporous and Mesoporous Materials*, 261, 79–87.
23. Mishra N.K.; Kumar C.; Kumar A.; Kumar M.; Chaudhary P.; Singh R. Structural and optical properties of SnO₂-Al₂O₃ Nanocomposite synthesized via sol-gel route. *Mater. Sci.-Pol.* 2015, 33, 714–718. <https://doi.org/10.1515/msp-2015-0101>
24. Imtiaz A.; Farrukh M.A.; Khaleeq-Ur-Rahman M.; Adnan R. Micelle-Assisted Synthesis of Al₂O₃-CaO Nanocatalyst: Optical Properties and Their Applications in Photodegradation of 2,4,6-Trinitrophenol. *Sci. World J.* 2013, 2013, 641420. <https://doi.org/10.1155/2013/641420> PMID: 24311980
25. Jong-Hwan Yoon (2019) "Fabrication of Sn@Al₂O₃ Core-shell Nanoparticles for Stable Nonvolatile Memory Applications" *Materials*, MDPI.
26. Hashmi Sidra, Gohar Sumbal, Mahmood Tariq, Nawaz Umar, Farooqi Hedayatullah (2016) "Biodiesel Production by using CaO-Al₂O₃ Nano Catalyst" *International Journal of Engineering Research & Science (IJOER)* ISSN: [2395–6992] [Vol- 2, Issue-3].
27. Cao K.; Zhu Q.; Shan B.; Chen R. Controlled synthesis of Pd/Pt core shell nanoparticles using area-selective atomic layer deposition. *Sci. Rep.* 2015, 5, 8470. <https://doi.org/10.1038/srep08470> PMID: 25683469
28. Wagner N.; Svensson A.-M.; Vullum-Bruer F. Effect of carbon content and annealing atmosphere on phase purity and morphology of Li₂MnSiO₄ synthesized by a P.V.A. assisted sol-gel method. *Solid State Ion.* 2015, 276, 26–32.
29. Wan J.Y.; Fan Y.; Yu Q.T.; Ge Y.Z.; Yan C.P.; Alolga R.N.; et al. Integrated evaluation of malonyl ginsenosides, amino acids and polysaccharides in fresh and processed ginseng. *J. Pharm. Biomed.* 2015, 107, 89–97.
30. Wan P.; Yang W.; Wang X.; Hu J.; Zhang H. Reduced graphene oxide modified with hierarchical flower-like In(OH)₃ for NO₂ room-temperature sensing. *Sens. Actuators B Chem.* 2015, 214, 36–42.
31. Abdulkarem E.; Ahmed I.; Abu-Zahra M.R.; Hasan S.W. Electrokinetic pretreatment of seawater to decrease the Ca²⁺, Mg²⁺, SO₄²⁻ and bacteria contents in membrane desalination applications. *Desalination* 2017, 403, 107–116.
32. Ahmadi M.; Baniyasi E.; Ahmadikia H. Process modeling and performance analysis of a productive water recovery system. *Appl. Therm. Eng.* 2017, 112, 100–110.
33. Reghioua A., Barkat D., Jawad A.H. et al. Magnetic Chitosan-Glutaraldehyde/Zinc Oxide/Fe₃O₄ Nanocomposite: Optimization and Adsorptive Mechanism of Remazol Brilliant Blue R Dye Removal. *J Polym Environ* 29, 3932–3947 (2021). <https://doi.org/10.1007/s10924-021-02160-z>
34. Ali Imran, Alharbi Omar M L, ALOthman Zeid A, Al-Mohaimed Amal Mohammed, Alwarthan Abdulrahman (2019) "Modeling of fenuron pesticide adsorption on C.N.T.s for mechanistic insight and removal in water" *Environ Res*; 170:389–397. Epub 2018 Dec 31. <https://doi.org/10.1016/j.envres.2018.12.066> PMID: 30623886

35. He Dong-Qin, Chen Jing-Yi, Bao Bo, Pan Xiang-Liang, Li Jun, Qian Chen, et al, (2019) "Optimizing sludge dewatering with a combined conditioner of Fenton's reagent and cationic surfactant" *Journal of Environmental Sciences*, P.P. 21–30, <https://doi.org/10.1016/j.jes.2019.08.009> PMID: 31862063
36. Bahrudin N. N., Nawati M. A., Jawad A. H., & Sabar S. (2020). Adsorption characteristics and mechanistic study of immobilized chitosan-montmorillonite composite for methyl orange removal. *Journal of Polymers and the Environment*, 28(7), 1901–1913. <https://doi.org/10.1007/s10924-020-01734-7>
37. Abd Malek N. N., Jawad A. H., Ismail K., Razuan R., & ALOthman Z. A. (2021). Fly ash modified magnetic chitosan-polyvinyl alcohol blend for reactive orange 16 dye removal: Adsorption parametric optimization. *International journal of biological macromolecules*, 189, 464–476. <https://doi.org/10.1016/j.ijbiomac.2021.08.160> PMID: 34450144
38. Ali I., Alharbi O. M., ALOthman Z. A., Al-Mohaimed A. M., & Alwarthan A. (2019). Modeling of fenuron pesticide adsorption on C.N.T.s for mechanistic insight and removal in water. *Environmental research*, 170, 389–397.
39. Dong D., Seo D., Seo S., & Lee J. W. (2018). Flocculation of microalgae using extracellular polymeric substances (EPS) extracted from activated sludge. *Membrane and Water Treatment*, 9(3), 147–153.
40. Ali I., Alharbi O. M., ALOthman Z. A., Al-Mohaimed A. M., & Alwarthan A. (2019). Modeling of fenuron pesticide adsorption on C.N.T.s for mechanistic insight and removal in water. *Environmental research*, 170, 389–397.
41. Dong D., Seo D., Seo S., & Lee J. W. (2018). Flocculation of microalgae using extracellular polymeric substances (EPS) extracted from activated sludge. *Membrane and Water Treatment*, 9(3), 147–153.
42. Wang J.; Qiu T.; Chen X.; Lu Y.; Yang W. N-doped carbon@Ni–Al₂O₃ nanosheet array@graphene oxide composite as an electrocatalyst for hydrogen evolution reaction in alkaline medium. *J. Power Sources* 2015, 293, 178–186.
43. Wang J.; Zhao G.; Jing L.; Peng X.; Li Y. Facile self-assembly of magnetite nanoparticles on three-dimensional graphene oxide–chitosan composite for lipase immobilization. *Biochem. Eng. J.* 2015, 98, 75–83.
44. Avithi Kanniappan S.; Ragula U.B.R. Effect of Reduction of Pt–Sn/α-Al₂O₃ on Catalytic Dehydrogenation of Mixed-Paraffin Feed. *Catalysts* 2020, 10, 113. <https://doi.org/10.3390/catal10010113>
45. Yoon J.-H. Fabrication of Sn@Al₂O₃ Core-shell Nanoparticles for Stable Nonvolatile Memory Applications. *Materials* 2019, 12, 3111. <https://doi.org/10.3390/ma12193111> PMID: 31554285
46. Wang H.; Yuan X.; Wu Y.; Chen X.; Leng L.; Wang H.; et al Facile synthesis of polypyrrole decorated reduced graphene oxide–Fe₃O₄ magnetic composites and its application for the Cr (VI) removal. *Chem. Eng. J.* 2015, 262, 597–606.
47. Kim Y.; Kim S. Direct growth of cobalt aluminum double hydroxides on graphene nanosheets and the capacitive properties of the resulting composites. *Electrochim. Acta* 2015, 163, 252–259.
48. Klučáková M.; Kalina M. Diffusivity of Cu(II) ions in humic gels—Influence of reactive functional groups of humic acids. *Colloids Surf. A Physicochem. Eng. Asp.* 2015, 483, 162–170.
49. Raudenský M.; Astrouski I.; Dohnal M. Intensification of heat transfer of polymeric hollow fiber heat exchangers by chaotisation. *Appl. Therm. Eng.* 2017, 113, 632–638.
50. Ma X.H.; Yang Z.; Yao Z.K.; Xu Z.L.; Tang C.Y. A facile preparation of novel positively charged M.O.F./chitosan nanofiltration membranes. *J. Membr. Sci.* 2017, 525, 269–276.
51. Matos Â.P.; Cavanholi M.G.; Moecke E.H.; Sant'Anna E.S. Effects of different photoperiod and trophic conditions on biomass, protein and lipid production by the marine alga *Nannochloropsis gaditana* at optimal concentration of desalination concentrate. *Bioresour. Technol.* 2017, 224, 490–497. <https://doi.org/10.1016/j.biortech.2016.11.004> PMID: 27839862
52. Ronen-Eliraz G., Russak A.; Nitzan I.; Guttman J.; Kurtzman D. Investigating geochemical aspects of managed aquifer recharge by column experiments with alternating desalinated water and groundwater. *Sci. Total Environ.* 2017, 574, 1174–1181. <https://doi.org/10.1016/j.scitotenv.2016.09.075> PMID: 27744262
53. Rafique M.M.; Rehman S. National energy scenario of Pakistan—Current status, future alternatives, and institutional infrastructure: An overview. *Renew. Sustain. Energy Rev.* 2017, 69, 156–167.
54. Yang M.; Zhao C.; Zhang S.; Li P.; Hou D. Preparation of graphene oxide modified poly(m-phenylene isophthalamide) nanofiltration membrane with improved water flux and antifouling property. *Appl. Surf. Sci.* 2017, 394, 149–159.
55. Yu W.; Tao J.; Yu X.; Zhao S.; Tu S.T.; Liu H. A microreactor with superhydrophobic Pt–Al₂O₃ catalyst coating concerning oxidation of hydrogen off-gas from fuel cell. *Appl. Energy* 2017, 185, 1233–1244.
56. Zhang B.; Hong J.G.; Xie S.; Xia S.; Chen Y. An integrative modeling and experimental study on the ionic resistance of ion-exchange membranes. *J. Membr. Sci.* 2017, 524, 362–369.

57. Tomaszekiewicz M.; Abou Najm M.; Zurayk R.; El-Fadel M. Dew as an adaptation measure to meet water demand in agriculture and reforestation. *Agric. For Meteorol.* 2017, 232, 411–421.
58. Barrett E.P.; Joyner L.G. Determination of nitrogen adsorption-desorption isotherms. *Anal. Chem.* 1951, 23, 791–792.
59. Vatanpour V.; Zoqi N. Surface modification of commercial seawater reverse osmosis membranes by grafting of hydrophilic monomer blended with carboxylated multiwalled carbon nanotubes. *Appl. Surf. Sci.* 2017, 396, 1478–1489.
60. Toral-Sánchez E.; Valdés J.A.; Aguilar C.N.; Cervantes F.J.; Rangel-Mendez J.R. Role of the intrinsic properties of partially reduced graphene oxides on the chemical transformation of iopromide. *Carbon* 2016, 99, 456–465.
61. Wang D.; Fang G.; Xue T.; Ma J.; Geng G. A melt route for the synthesis of activated carbon derived from carton box for high performance symmetric supercapacitor applications. *J. Power Sources* 2016, 307, 401–409.
62. Abuhatab S.; El-Qanni A.; Al-Qalaq H.; Hmoudah M.; Al-Zerei W. Effective adsorptive removal of Zn²⁺, Cu²⁺, and Cr³⁺ heavy metals from aqueous solutions using silica-based embedded with NiO and MgO nanoparticles. *J. Environ. Manag.* 2020, 268, 110713.
63. Fang Y.; Lv X.; Xu X.; Zhu J.; Liu P.; Guo L.; et al. Three-dimensional nanoporous starch-based material for fast and highly efficient removal of heavy metal ions from wastewater. *Int. J. Biol. Macromol.* 2020, 164, 415–426. <https://doi.org/10.1016/j.ijbiomac.2020.07.017> PMID: 32663560
64. Liu W.; Zhang J.; Jin Y.; Zhao X.; Cai Z. Adsorption of Pb (II), Cd (II) and Zn (II) by extracellular polymeric substances extracted from aerobic granular sludge: Efficiency of protein. *J. Environ. Chem. Eng.* 2015, 3, 1223–1232.
65. Roy A. Microwave-assisted Synthesis and characterization of γ -Al₂O₃/ γ -Fe₂O₃ composite and evaluating its efficiency in fluoride removal. *Colloids Surf. A Physicochem. Eng. Asp.* 2021, 608, 125574.
66. Soleymanzadeh M.; Arshadi M.; Salvacion J.W.; SalimiVahid F. A new and effective nanobiocomposite for sequestration of Cd (II) ions: Nanoscale zerovalent iron supported on sineguelas seed waste. *Chem. Eng. Res. Des.* 2015, 93, 696–709.
67. Jacundino J.S.; Santos O.S.; Santos J.C.; Botero W.G.; Goveia D.; do Carmo J.B.; et al. Interactions between humin and potentially toxic metals: Prospects for its utilization as an environmental repair agent. *J. Environ. Chem. Eng.* 2015, 3, 708–715.
68. Xue X.; Xu J.; Baig S.A.; Xu X. Synthesis of graphene oxide nanosheets for the removal of Cd (II) ions from acidic aqueous solutions. *J. Taiwan Inst. Chem. Eng.* 2016, 59, 365–372.
69. Mubarak M.F.; Ragab A.H.; Hosny R.; Ahmed I.A.; Ahmed H.A.; El-Bahy S.M.; et al. Enhanced Performance of Chitosan via a Novel Quaternary Magnetic Nanocomposite Chitosan/Grafted Halloysitenanotubes@ Zn₂Fe₃O₄ for Uptake of Cr (III), Fe (III), and Mn (II) from Wastewater. *Polymers* 2021, 13, 2714.
70. El Shahawy A.; Ragab A.H.; Mubarak M.F.; Ahmed I.A.; Mousa A.E.; Bader D.M. Removing the Oxamyl from Aqueous Solution by a Green Synthesized HTiO₂@ AC/SiO₂ Nanocomposite: Combined Effects of Adsorption and Photocatalysis. *Catalysts* 2022, 12, 163.
71. Raval N.P.; Shah P.U.; Shah N.K. Adsorptive removal of Nickel(II) ions from aqueous environment: A review. *J. Environ. Manag.* 2016, 179, 1–20. <https://doi.org/10.1016/j.jenvman.2016.04.045> PMID: 27149285
72. Ren M.; Yang M.; Liu W.; Li M.; Su L.; Qiao C.; et al. Ultra-small Fe₃O₄ nanocrystals decorated on 2D graphene nanosheets with excellent cycling stability as anode materials for lithium ion batteries. *Electrochim. Acta* 2016, 194, 219–227.
73. Achary M.S.; Satpathy K.K.; Panigrahi S.; Mohanty A.K.; Padhi R.K.; Biswas S.; et al. Concentration of heavy metals in the food chain components of the nearshore coastal waters of Kalpakkam, southeast coast of India. *Food Control* 2017, 72, 232–243.
74. Adams J.; Bighane N.; Koros W.J. Pore morphology and temperature dependence of gas transport properties of silica membranes derived from oxidative thermolysis of polydimethylsiloxane. *J. Membr. Sci.* 2017, 524, 585–595.
75. Wang X.; Zhang Y.; Li J.; Zhang G.; Li X. Enhance Cr (VI) removal by quaternary amine-anchoring activated carbons. *J. Taiwan Inst. Chem. Eng.* 2016, 58, 434–440.
76. Wang H.; Yu W.; Mao N.; Shi J.; Liu W. Effect of surface modification on high-surface-area carbon nanosheets anode in sodium ion battery. *Microporous Mesoporous Mater.* 2016, 227, 1–8.
77. Manirethan V.; Raval K.; Rajan R.; Thaira H.; Balakrishnan R.M. Kinetic and thermodynamic studies on the adsorption of heavy metals from aqueous solution by melanin nanopigment obtained from marine source: *Pseudomonas stutzeri*. *J. Environ. Manag.* 2018, 214, 315–324. <https://doi.org/10.1016/j.jenvman.2018.02.084> PMID: 29533829

78. Kasprzyk-Hordern B. Chemistry of alumina, reactions in aqueous solution and its application in water treatment. *Adv. Colloid Interface Sci.* 2004, 110, 19–48. <https://doi.org/10.1016/j.cis.2004.02.002> PMID: 15142822
79. Zhan J.; Wang H.; Pan X.; Wang J.; Yu G.; Deng S.; et al. Simultaneous regeneration of p-nitrophenol-saturated activated carbon fiber and mineralization of desorbed pollutants by electro-peroxone process. *Carbon* 2016, 101, 399–408.
80. Xing M.; Xu L.; Wang J. Mechanism of Co(II) adsorption by zerovalent iron/graphene nanocomposite. *J. Hazard. Mater.* 2016, 301, 286–296. <https://doi.org/10.1016/j.jhazmat.2015.09.004> PMID: 26368802
81. Xie Y.; Song J.; Zhou P.; Ling Y.; Wu Y. Controllable synthesis of TiO₂/graphene nanocomposites for long lifetime lithium storage: Nanoparticles vs. nanolayers. *Electrochim. Acta* 2016, 210, 358–366.
82. Liu D.; Li Z.; Li W.; Zhong Z.; Xu J.; Ren J.; et al. Adsorption behavior of heavy metal ions from aqueous solution by soy protein hollow microspheres. *Ind. Eng. Chem. Res.* 2013, 52, 11036–11044.
83. Kyzas G.Z.; Sifaka P.I.; Lambropoulou D.A.; Lazaridis N.K.; Bikiaris D.N. Poly (itaconic acid)-grafted chitosan adsorbents with different cross-linking for Pb (II) and Cd (II) uptake. *Langmuir* 2014, 30, 120–131. <https://doi.org/10.1021/la402778x> PMID: 24011255
84. Mohammed C.; Mahabir S.; Mohammed K.; John N.; Lee K.Y.; Ward K. Calcium alginate thin films derived from *Sargassum natans* for the selective adsorption of Cd²⁺, Cu²⁺, and Pb²⁺ ions. *Ind. Eng. Chem. Res.* 2018, 58, 1417–1425.
85. Kweon D.K.; Choi J.K.; Kim E.K.; Lim S.T. Adsorption of divalent metal ions by succinylated and oxidized corn starches. *Carbohydr. Polym.* 2001, 46, 171–177.
86. Ibrahim B.M.; Fakhre N.A. Crown ether modification of starch for adsorption of heavy metals from synthetic wastewater. *Int. J. Biol. Macromol.* 2019, 123, 70–80. <https://doi.org/10.1016/j.ijbiomac.2018.11.058> PMID: 30439424
87. Akinterinwa A.; Oladele E.; Adebayo A.; Gurgur E.; Iyanu O.O.; Ajayi O. Cross-linked-substituted (esterified/etherified) starch derivatives as aqueous heavy metal ion adsorbent: A review. *Water Sci. Technol.* 2020, 82, 1–26. <https://doi.org/10.2166/wst.2020.332> PMID: 32910789